Optical Signatures of Hydration-Controlled Hysteretic Spin crossover in Single Crystals of an Fe(II) Complex

Chinmoy Das[1], Malcolm A. Halcrow[2], Denisa Coltuneac[3], Laurentiu Stoleriu[3],
Pradip Chakraborty[1]*

[1]Department of Chemistry, Indian Institute of Technology Kharagpur, Kharagpur-721302, India

[2]School of Chemistry, University of Leeds, Woodhouse Lane, Leeds, UK LS2 9JT

[3]Faculty of Physics, Al. I. Cuza University, 700506 Iasi, Romania

*Corresponding Author, E-mail: pradipc@chem.iitkgp.ac.in

Abstract

This study presents a comprehensive optical spectroscopic investigation of spin-crossover (SCO) behavior in the Fe(II) complex, $[Fe(bppsipr)_2](BF_4)_2$ (where bppsipr = 4-(isopropylsulfanyl)-2,6-bis(pyrazol-1-yl)pyridine), in both hydrated and dehydrated single-crystal forms. High-resolution single-crystal UV-Vis absorption spectroscopy is employed to monitor thermally driven spin-state switching at multiple temperature scan rates, revealing abrupt transitions with variable hysteresis widths. In the hydrated form, hysteresis width narrowed with decreasing scan rate due to reduced kinetic barriers and variation in cooperativity. Incontrast, the dehydrated form displayed stronger scan-rate dependence, wider hysteresis, and metastable high-spin (HS) stabilization upon cooling, attributed to increased lattice rigidity, and elevated relaxation barriers. Notably, the mutual interplay between elastic and magnetic interactions differ between cooling (HS → LS) and heating (LS → HS) cycles across scan rates. Thermal annealing of the dehydrated crystal restored structural homogeneity, yielding narrower hysteresis and upward-shifted transition temperatures during cooling, without affecting the heating branch–indicating asymmetric energy dissipation dynamics (magnetic *vs* elastic) during HS → LS and LS → HS transitions. The hydrated compound also demonstrates efficient photoinduced LS → HS switching (LIESST) at 4 K, with metastable HS state relaxing sharply near T(LIESST). Time-resolved spectroscopy between 50-75 K revealed two-step HS → LS relaxation mechanism, involving initial stochastic LS nucleation followed by cooperative domain growth. In contrast, no photoresponse is observed in the dehydrated form within measurement timeframe, likely due to increased ΔE^0_{HL} and higher lattice stiffness. Partial LS recovery *via* reverse-LIESST (830 nm excitation) confirms bistability and domain sensitivity in the hydrated state. To model the photoinduced relaxation behavior, an advanced mechanoelastic framework is applied, integrating thermodynamic, elastic, and local structural factors including hydration-induced pressure and Jahn-Teller distortion. The model successfully reproduced the cooperative HS → LS relaxation kinetics and domain evolution, validating the significance of local pressure fluctuations, lattice inhomogeneities, and angular strain in dictating SCO dynamics. Overall, this work highlights the critical influence of hydration-dehydration, lattice quality, and thermal history on spin-state cooperativity and bistability, offering deep insight into the molecular control of SCO behavior. The integrated experimental-theoretical approach offers valuable insights for designing next-generation photoresponsive SCO materials with tunable switching characteristics.

Introduction

Spin-crossover (SCO) materials have garnered increasing attention for their potential applications in data storage, memory devices, sensors, and biomedical systems. These compounds, typically featuring transition metals with $3d^4$ to $3d^7$ electronic configurations, undergo reversible switching between low-spin (LS) and high-spin (HS) states in response to external stimuli such as temperature, light, pressure, magnetic or electric fields.[1-6] Among SCO systems, Fe(II)-based complexes are the most widely studied. They display a thermally driven transition from a diamagnetic LS state ($S = 0$, $t_{2g}^6e_g^0$, $^1A_1$) to a paramagnetic HS state ($S = 2$, $t_{2g}^4e_g^2$, $^5T_2$), primarily governed by the zero-point energy difference (ΔE^0_{HL}) between the spin states.[6] This entropy-driven transition involves a significant ~ 0.2 Å elongation of the metal−ligand bonds, resulting in changes to the coordination sphere volume and elastic properties. The character of the transition-whether gradual, abrupt, or multistep-is dictated by factors such as ligand field strength, crystal packing, and host-guest interactions.[6,7] Gradual transitions typically reflect non-cooperative, Boltzmann-type behavior with independently switching centers, while abrupt transitions-often displaying thermal hysteresis-indicate strong cooperative interactions and bistability.[8]

Thermal hysteresis in SCO systems introduces a memory effect, making them attractive for switching and memory device applications. This hysteresis commonly arises from cooperativity, which stems from short- and long-range interactions among spin centers.[8] Coordination polymers, where SCO centers are covalently linked, often exhibit stronger cooperativity-and thus wider hysteresis loops-than molecular crystals held together by weaker hydrogen bonding or van der Waals forces. These cooperative interactions can lead to first-order phase transitions with pronounced changes in magnetic, optical, and structural properties.[9]

Beyond thermal spin transitions, SCO systems can also be controlled through wavelength-selective light irradiation. At low temperatures, the LS ($^1A_1$) ground state can be photoexcited into a metastable HS ($^5T_2$) state via metal-to-ligand charge transfer (MLCT) or d-d transitionsa process known as Light-Induced Excited Spin-State Trapping (LIESST).[10-15] The reverse transition, restoring the LS state from the photoinduced HS state using light, is referred to as reverse-LIESST.[12,16-18] These photoresponsive behaviors expand the functional versatility of SCO materials, particularly under out-of-equilibrium conditions.

A key parameter in this context is T(LIESST) − the limit temperature above which the photoinduced metastable HS state is erased and thermally reverts back to the LS state.[19-21] T(LIESST) reflects the dynamic stability of the photoexcited state and is often inversely correlated with the thermal transition temperature ($T_{½}$) through Hauser's inverse energy gap law.[12] The relaxation dynamics of the metastable HS state thus provide insights into the complex interplay between molecular structure, lattice cooperativity, and out-of-equilibrium SCO behavior.[12,22-26]

Solvation plays a crucial role in modulating SCO behavior by influencing crystal packing, intermolecular interactions, and lattice dynamics.[27,28] For example, Harding et al. and McMurtrie et al. have shown that symmetry breaking and solvent effects play a crucial role in governing the photoswitchability and spin-state dynamics of Fe(III) complexes.[29,30] Ruben et al. showed that removing CH_3CN from the lattice reduces hysteresis width and weakens cooperativity.[31] Halcrow et al. reported that desolvation can trigger single-crystal-to-single-crystal transformations, altering spin-state behavior through structural rearrangement.[32] Shatruk and co-workers also observed shifts in $T_{½}$ upon solvent loss, emphasizing the environmental sensitivity of SCO systems.[33] Expanding on these findings, Halcrow and collaborators studied $[Fe(1\text{-bpp})_2]X_2$ complexes (X = ClO_4^-, BF_4^-) bearing 4-(isoalkylsulfanyl) substituents and various lattice solvents (e.g., CH_3CN, $(CH_3)_2CO$, EtCN, H_2O, $MeNO_2$).[34-36] These complexes displayed diverse SCO profiles influenced by both the counter-ions and solvents. Notably, the hydrated complex $[Fe(bppsipr)_2](BF_4)_2 \cdot H_2O$ exhibits a sharp spin transition with narrow thermal hysteresis ($T_{½}\downarrow = 210$ K, $T_{½}\uparrow = 214$ K). Upon desolvation, the transition shifts to lower temperatures ($T_{½}\downarrow = 182$ K, $T_{½}\uparrow = 188$ K), indicating HS state stabilization.[34] The hydrated form also shows a T(LIESST) of 80 K, though the photoresponse of the desolvated analogue remains unreported.

Single-crystal optical spectroscopy, though highly sensitive to crystal quality, dimensions, and color, offers unique insights not accessible by other techniques. It provides detailed information on the electronic structure, including ligand-field and charge-transfer energies and band intensities,[12] while also detecting baseline shifts from diffuse scattering linked to domain formation during phase transitions.[37] Interference patterns reveal crystal defects or microcracks from thermal cycling,[37] and wavelength-selective measurements directly quantify spin-state switching via LIESST, reverse-LIESST, and optical bistability.[12,37,38] It tracks spin-cluster nucleation, growth, and front propagation,[39-41] light-induced phase separation and transitions,[42-44] and ultrafast excited-state dynamics such as intersystem crossing, vibrational cooling, and internal conversion.[44-48] Furthermore, it enables fundamental mechanistic insights into cooperative effects[49,50] and distinguishes thermally, light-, and pressure-induced spin-state switching across crystals, powders, and thin films.[51,52]

Therefore, to deepen our understanding of how solvation influences both thermal and photoinduced SCO behavior, we present what is, to the best of our knowledge, the first comprehensive optical spectroscopy-based study of a Fe(II) SCO single-crystalline solid undergoing an isostructural single-crystal-to-single-crystal transformation between its hydrated and dehydrated forms. This system displays pronounced temperature sweep rate-dependent thermal hysteresis and robust photoinduced spin switching.

Our investigation integrates temperature-dependent, high-resolution single-crystal absorption spectroscopy with spin-transition measurements conducted under variable temperature ramp rates. We further explore the Light-Induced Excited Spin-State Trapping (LIESST) effect, determine the associated T(LIESST), and evaluate the relaxation dynamics of the metastable HS state across a range of temperatures. The observed relaxation behavior is consistently interpreted within the framework of the mechanoelastic model, offering valuable insights into the interplay between solvation, lattice dynamics, and SCO cooperativity- highlighting the novelty and relevance of this work.

Experimental

High-quality yellow rod-shaped single crystals were obtained following a previously reported crystallization procedure.[34] A representative image is provided in the Supporting Information (Figure S1).

Optical Measurement:

At room temperature, the single crystals appear yellow, turning dark red upon cooling (Figure S2), indicative of a thermally induced spin-state transition. For optical studies, a crystal measuring approximately $0.38 \times 0.25 \times 0.12$ mm^3 was selected, with its thickness optimized to avoid absorption saturation and baseline distortion. The crystal was mounted on a copper plate with a 0.2 mm hole using silver paste to ensure efficient thermal contact for both thermal and photoinduced measurements. The setup was placed in a helium-cooled, vacuum-sealed closed-cycle cryostat (Model: RDK-101J) equipped with a Lakeshore 335 temperature controller, operating from 4 to 450 K. Variable-temperature absorption spectra were recorded in the 400-

800 nm range using a high-resolution dual-beam UV–Vis–NIR spectrometer (Agilent Cary 5000), under various temperature sweep rates to monitor thermal spin transitions. For LIESST experiments, the sample was cooled to 4 K and irradiated with a 632 nm continuous-wave HeNe laser (2 mW/ mm^2) for five minutes. T(LIESST) was determined by heating the sample at 0.3 K/min post-irradiation while recording spectra to track relaxation from the photoinduced HS state. For photoinduced relaxation dynamics, the sample was irradiated at 4 K, rapidly heated at 10 K/min to the target temperature, held isothermally, and monitored over time to capture the bleaching of the metastable HS state.

Results and discussion

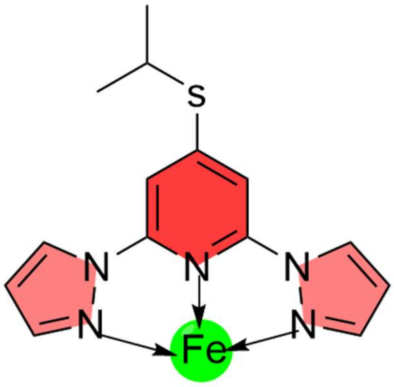

Scheme 1. Chemical structure and coordination mode of 4-{iso-propylsulfanyl}-2,6 di{pyrazol-1-yl}pyridine (bppsipr) in the [Fe(bppsipr)$_2$](BF$_4$)$_2$ compound. The arrows indicate the nitrogen donor atoms involved in coordination to the Fe(II) center.

Scheme 1 illustrates the chemical structure and coordination motif of the 4-(isopropylsulfanyl)-2,6-bis(pyrazol-1-yl)pyridine ligand. This molecule is built on a 2,6-bis(pyrazol-1-yl)pyridine scaffold, with an iso-propylsulfanyl group substituted at the 4-position of the pyridine ring.34 The ligand acts as a tridentate donor, as indicated by the arrows in Scheme 1, coordinating through two pyrazole and one pyridine nitrogen atoms. Coordination of two such ligands to an Fe(II) center results in a pseudo-octahedral geometry, constrained by the ligand's backbone. From an electronic structure perspective, the ligand plays a crucial role in governing the SCO behavior of the Fe(II) complex. It influences not only the ligand field strength but also contributes to the overall crystal packing and the nature of intermolecular interactions. These include electrostatic forces, hydrogen bonding, π-π stacking, and other dipolar or quadrupolar interactions involving the cationic complex, counter-anions, and lattice components-factors that collectively modulate the SCO properties.

Both the hydrated $[Fe(bppsipr)_2](BF_4)_2.H_2O$ and dehydrated $[Fe(bppsipr)_2](BF_4)_2$ complexes crystallize in the monoclinic space group $P2_1/c$ with Z = 4, consistent with the structure previously reported by Halcrow et al.[34] In both cases, the Fe(II) center is coordinated by two tridentate bppsipr ligands, forming a slightly distorted octahedral geometry − a typical coordination pattern observed in $[Fe(1\text{-}bpp)_2]^{2+}$ systems.[53-55] In the HS state, the complex exhibits angular Jahn-Teller distortion due to orbital degeneracy, leading to deviations from ideal octahedral symmetry. Conversely, the LS state, which is orbitally non-degenerate, adopts a more symmetric geometry. In this state, the bppsipr ligands approach a nearly perpendicular arrangement, with trans angles close to 180° and dihedral angles near 90°, as previously reported.[56] The HS-to-LS spin transition is thus accompanied by a shift in molecular geometry from a distorted to a nearly undistorted configuration-which affects the shape of individual molecules without significantly altering the overall crystal lattice.[54] In the hydrated form, the crystal structure confirms the presence of a single lattice water molecule. This solvent can be readily removed by heating above 350 K, yielding the structurally similar dehydrated phase.

Thermal spin transition behavior:

Figures 1-3 present high-resolution single-crystal UV-Vis absorption spectra of $[Fe(bppsipr)_2](BF_4)_2$ in its hydrated (with one lattice H_2O molecule), dehydrated, and annealed-dehydrated forms, respectively. Spectra are recorded during both cooling and heating cycles at varying temperature scan rates: 1 K/min (Figures 1a-b, 2a-b, 3a-b), 0.5 K/min (Figures 1c-d, 2c-d, 3c-d), 0.25 K/min (Figures 1e-f, 2e-f), 0.1 K/min (Figures 1g-h, 2g-h), and 0.05 K/min (Figures 1i-j, 2i-j). Measurements are performed with incident light perpendicular to the crystal surface. Although the full spectral range is 400-800 nm, only the 450-800 nm region is displayed for clarity.

To prepare the dehydrated form, single crystal is heated under high vacuum to 390 K and held for one hour. In subsequent thermal cycles, the dehydrated sample is annealed at 350 K between cycles to eliminate defects induced by spin-state switching and thermal stress. The comparison of hydrated, dehydrated, and annealed-dehydrated crystals at different scan rates provides critical insights into the roles of lattice defects, packing, structural reorganization, and the presence or absence of lattice water. These factors influence key SCO characteristics, including cooperativity, transition abruptness, hysteresis width, and activation barriers for relaxation.

Each spectral set tracks the evolution of metal-to-ligand charge transfer (MLCT) bands during the thermal spin transition. The MLCT bands, with strong absorption ($\varepsilon \sim 10{,}000$ L mol^{-1} cm^{-1}), dominate over the weaker ligand-field (d-d) transitions ($\varepsilon \sim 100$–200 L mol^{-1} cm^{-1}). In the LS state, the 1A1 → 1MLCT transition appears as a broad shoulder between 630–675 nm. In the HS state, the corresponding $^5T_2 \rightarrow {}^5$MLCT transition is blue-shifted and manifests around 450–500 nm. Below this region, both MLCT bands become saturated. Additionally, a weak $^5T_2 \rightarrow {}^5E$ d-d band (~800 nm, $\varepsilon \sim 10$-40 L mol^{-1} cm^{-1}) appears inconsistently due to low detector sensitivity and is unsuitable for precise tracking of spin-state conversion.

To monitor the spin transition, absorbance at 640 nm is used-where the LS state shows a strong shoulder, while the HS state exhibits minimal absorbance (indicated by dashed lines in each spectrum of Figures 1, 2, and 3). This differential response enables quantitative determination of the temperature-dependent high-spin fraction (γ_{HS}), normalized against fully LS and HS reference states (Figures 4 and 5). As temperature decreases, the HS ^{5}MLCT band weakens and red-shifts, signaling depopulation of the HS state and emergence of the stronger LS ^{1}MLCT band, which is red-shifted due to enhanced metal–ligand orbital overlap and shorter Fe–N bond lengths.

Importantly, most spectra show no baseline shifts during thermal cycling, indicating the absence of crystallographic phase transitions-except in Figure 3c, where a minor baseline offset may result from diffuse scattering caused by domain formation or subtle packing rearrangements. Such scattering typically occurs when domain sizes approach the wavelength of incident light. Notably, in the hydrated (Figure 1h–j) and dehydrated (Figure 2) single crystals at the slowest scan rates, interference patterns appear without significant baseline shifts. This likely arises from crystal defects or micro-cracks formed during repeated thermal cycling, which are notably absent in the annealed-dehydrated spectra (Figure 3).

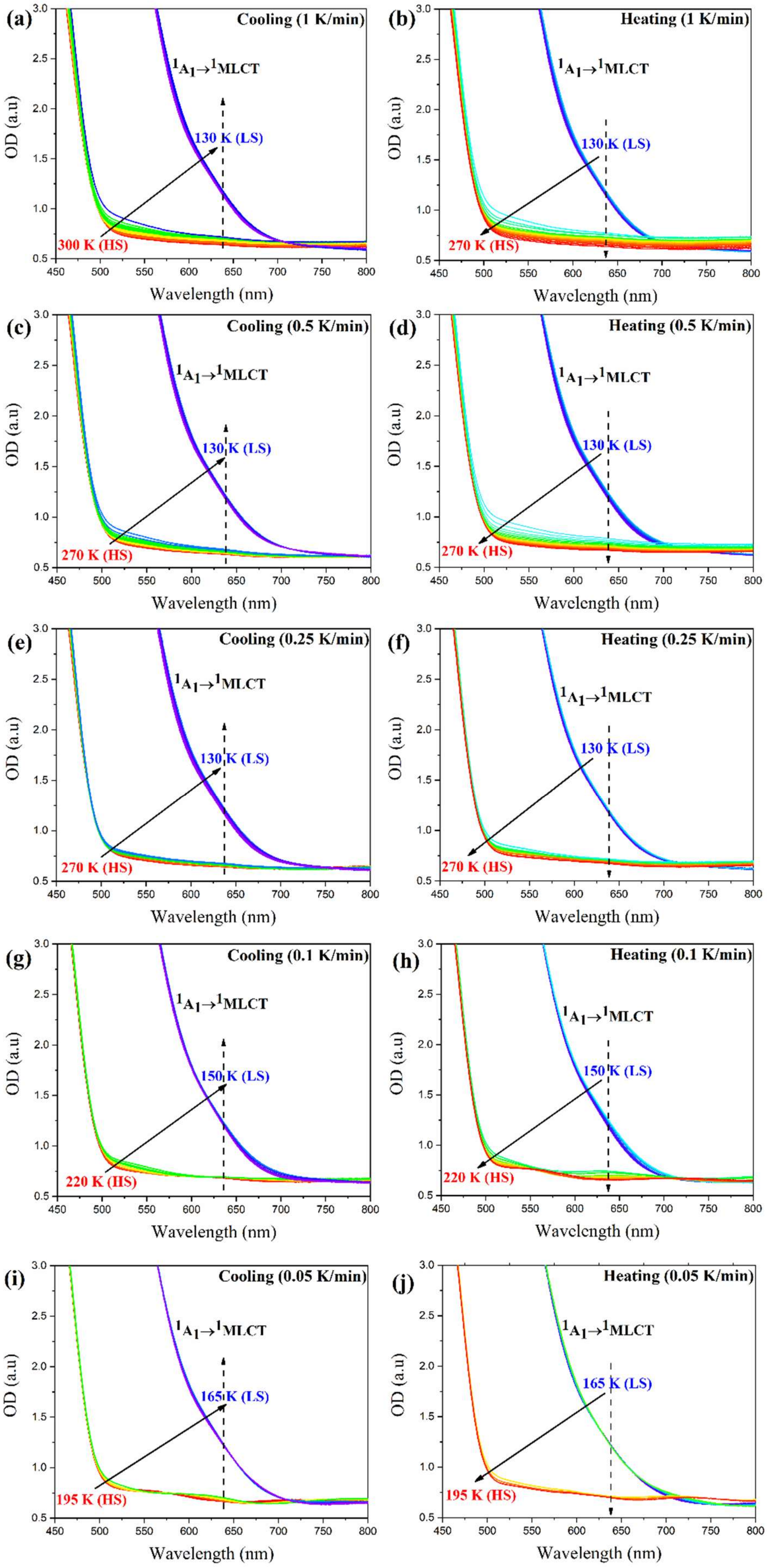
(a)
Cooling (1 K/min)
$^1A_1 \rightarrow {}^1MLCT$
130 K (LS)
300 K (HS)
(b)
Heating (1 K/min)
$^1A_1 \rightarrow {}^1MLCT$
130 K (LS)
270 K (HS)
(c)
Cooling (0.5 K/min)
$^1A_1 \rightarrow {}^1MLCT$
130 K (LS)
270 K (HS)
(d)
Heating (0.5 K/min)
$^1A_1 \rightarrow {}^1MLCT$
130 K (LS)
270 K (HS)
(e)
Cooling (0.25 K/min)
$^1A_1 \rightarrow {}^1MLCT$
130 K (LS)
270 K (HS)
(f)
Heating (0.25 K/min)
$^1A_1 \rightarrow {}^1MLCT$
130 K (LS)
270 K (HS)
(g)
Cooling (0.1 K/min)
$^1A_1 \rightarrow {}^1MLCT$
150 K (LS)
220 K (HS)
(h)
Heating (0.1 K/min)
$^1A_1 \rightarrow {}^1MLCT$
150 K (LS)
220 K (HS)
(i)
Cooling (0.05 K/min)
$^1A_1 \rightarrow {}^1MLCT$
165 K (LS)
195 K (HS)
(j)
Heating (0.05 K/min)
$^1A_1 \rightarrow {}^1MLCT$
165 K (LS)
195 K (HS)
OD (a.u)
0.5
1.0
1.5
2.0
2.5
3.0
Wavelength (nm)
450
500
550
600
650
700
750
800

Figure 1. Temperature-dependent high-resolution single-crystal UV-Vis absorption spectra of hydrated [Fe(bppsipr)$_2$](BF$_4$)$_2$.H$_2$O recorded during (left panels) cooling and (right panels) heating cycles at scan rates of (**a-b**) 1 K/min, (**c-d**) 0.5 K/min, (**e-f**) 0.25 K/min, (**g-h**) 0.1 K/min, and (**i-j**) 0.05 K/min. Spectra are color-coded using a rainbow gradient to indicate intermediate temperatures. Solid arrows denote the direction of spin-state switching, while dashed arrows (upward for cooling, downward for heating) highlight the spectral regions used to monitor the spin-state evolution.

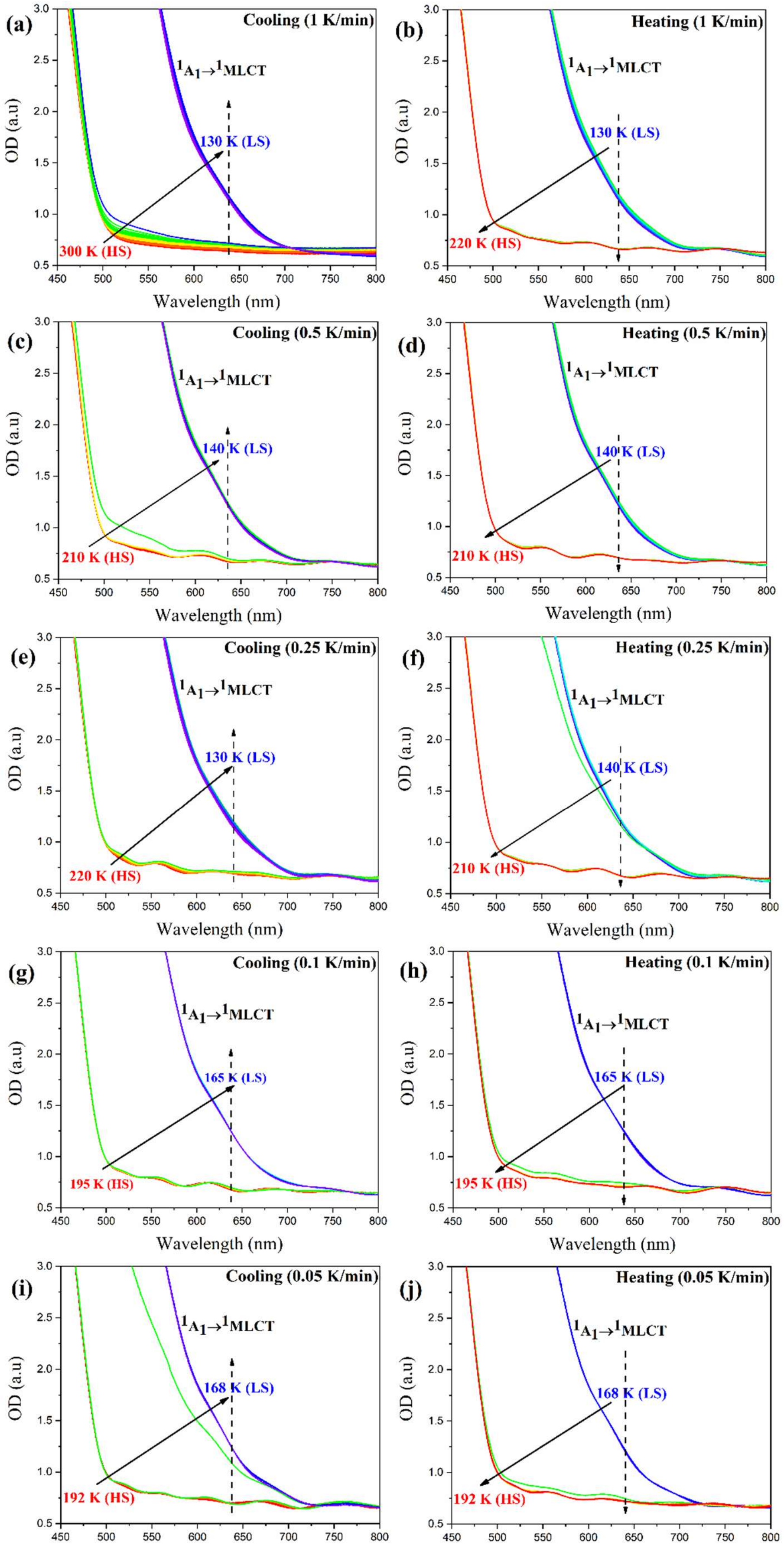
(a)
Cooling (1 K/min)
$^1A_1 \rightarrow ^1MLCT$
130 K (LS)
300 K (HS)
(b)
Heating (1 K/min)
$^1A_1 \rightarrow ^1MLCT$
130 K (LS)
220 K (HS)
(c)
Cooling (0.5 K/min)
$^1A_1 \rightarrow ^1MLCT$
140 K (LS)
210 K (HS)
(d)
Heating (0.5 K/min)
$^1A_1 \rightarrow ^1MLCT$
140 K (LS)
210 K (HS)
(e)
Cooling (0.25 K/min)
$^1A_1 \rightarrow ^1MLCT$
130 K (LS)
220 K (HS)
(f)
Heating (0.25 K/min)
$^1A_1 \rightarrow ^1MLCT$
140 K (LS)
210 K (HS)
(g)
Cooling (0.1 K/min)
$^1A_1 \rightarrow ^1MLCT$
165 K (LS)
195 K (HS)
(h)
Heating (0.1 K/min)
$^1A_1 \rightarrow ^1MLCT$
165 K (LS)
195 K (HS)
(i)
Cooling (0.05 K/min)
$^1A_1 \rightarrow ^1MLCT$
168 K (LS)
192 K (HS)
(j)
Heating (0.05 K/min)
$^1A_1 \rightarrow ^1MLCT$
168 K (LS)
192 K (HS)
OD (a.u)
3.0
2.5
2.0
1.5
1.0
0.5
Wavelength (nm)
450
500
550
600
650
700
750
800

Figure 2. Temperature-dependent high-resolution single-crystal UV-Vis absorption spectra of hydrated [Fe(bppsipr)$_2$](BF$_4$)$_2$ recorded during (left panels) cooling and (right panels) heating cycles at scan rates of (**a-b**) 1 K/min, (**c-d**) 0.5 K/min, (**e-f**) 0.25 K/min, (**g-h**) 0.1 K/min, and (**i-j**) 0.05 K/min. Spectra are color-coded using a rainbow gradient to indicate intermediate temperatures. Solid arrows denote the direction of spin-state switching, while dashed arrows (upward for cooling, downward for heating) highlight the spectral regions used to monitor the spin-state evolution.

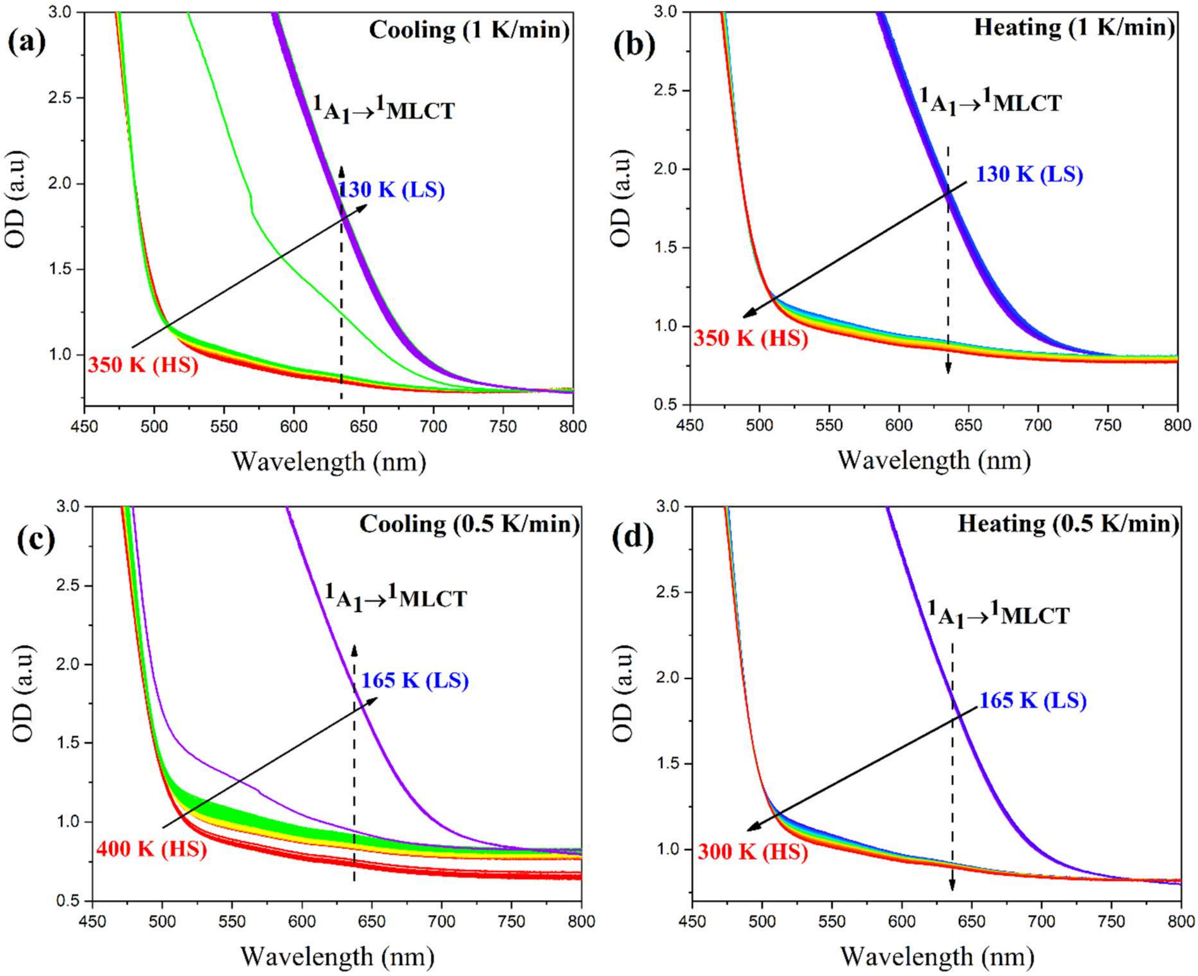

Figure 3. Temperature-dependent high-resolution single-crystal UV-Vis absorption spectra of annealed dehydrated $[Fe(bppsipr)_2](BF_4)_2$ recorded during cooling (left panels) and heating (right panels) cycles at scan rates of (**a-b**) 1 K/min and (**c-d**) 0.5 K/min. Spectra are color-coded using a rainbow gradient to represent intermediate temperatures. Solid arrows indicate the direction of spin-state switching, while dashed arrows (upward during cooling and downward during heating) highlight the spectral regions used to monitor spin-state evolution with temperature.

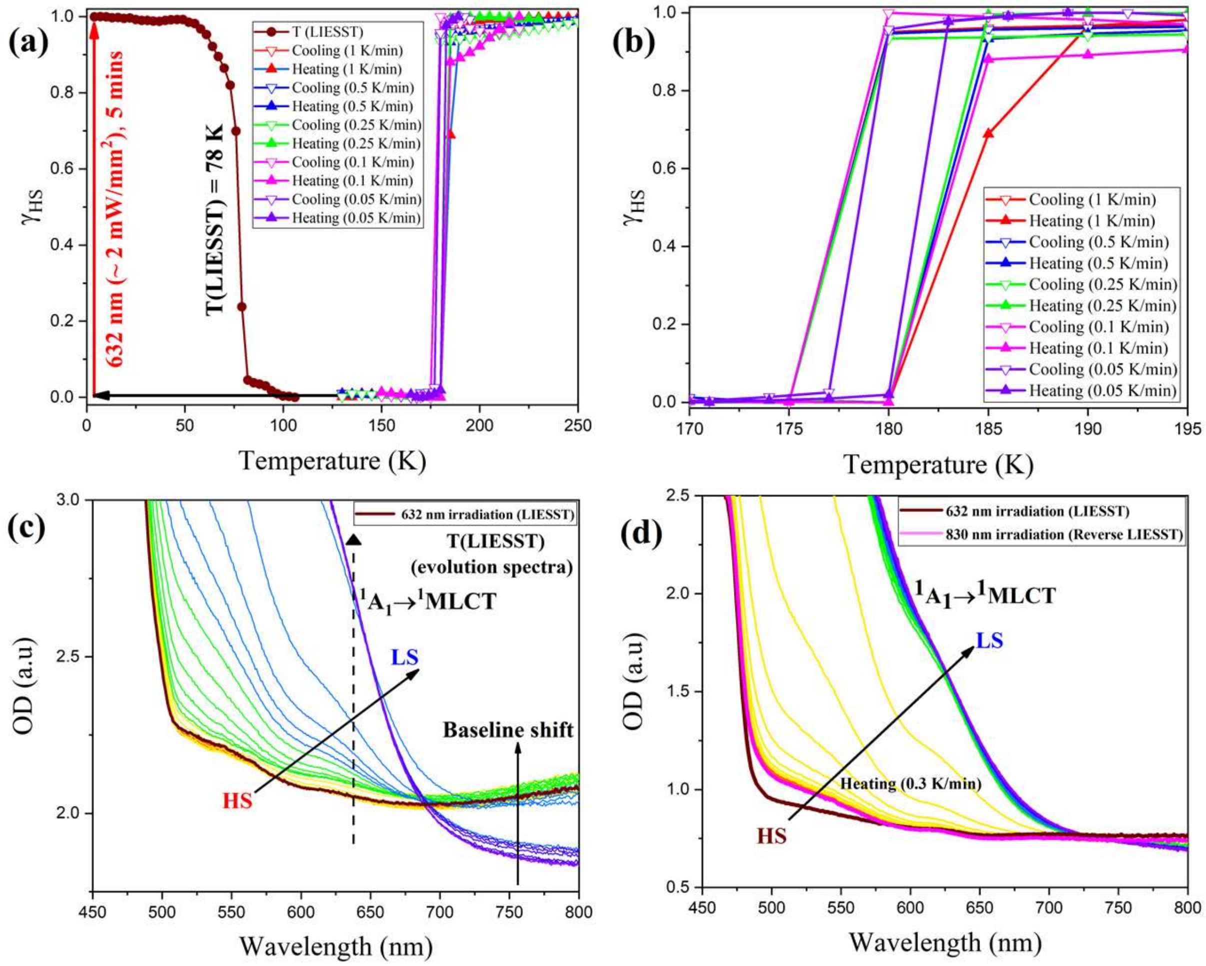

Figure 4. (a) Thermal spin-transition curves of hydrated $[Fe(bppsipr)_2](BF_4)_2.H_2O$ obtained from high-quality single-crystal UV-Vis absorption measurements during cooling (open downward triangles) and heating (solid upward triangles) at various temperature scan rates: 1 K/min (red), 0.5 K/min (blue), 0.25 K/min (light green), 0.1 K/min (pink), and 0.05 K/min (violet). The T(LIESST) curve (brown solid circles) was recorded following irradiation with 632 nm light (~2 mW/mm^2, red upward arrow) at 4 K for five minutes, then warming at 0.3 K/min. A black horizontal arrow connects the T(LIESST) and thermal transition curves at γ_{HS} = 0. **(b)** Enlarged view of the thermal spin-transition region between 170 K and 195 K, with color coding corresponding to panel (a). **(c)** Temperature-dependent spectral evolution during the T(LIESST) experiment. The post-irradiation spectrum at 4 K is shown in dark brown. Dashed arrows indicate spectral regions used to monitor spin-state changes with temperature. **(d)** Spectral evolution during the reverse-LIESST process, showing partial recovery from the LIESST-induced HS state (dark brown) to a ~10% reconverted LS state (pink). A solid black arrow highlights the baseline shift near 750 nm. In both **(c)** and **(d)**, the emergence and

intensification of the $^1A_1 \rightarrow {}^1MLCT$ band signal the re-establishment of the LS state, as marked by solid black arrows.

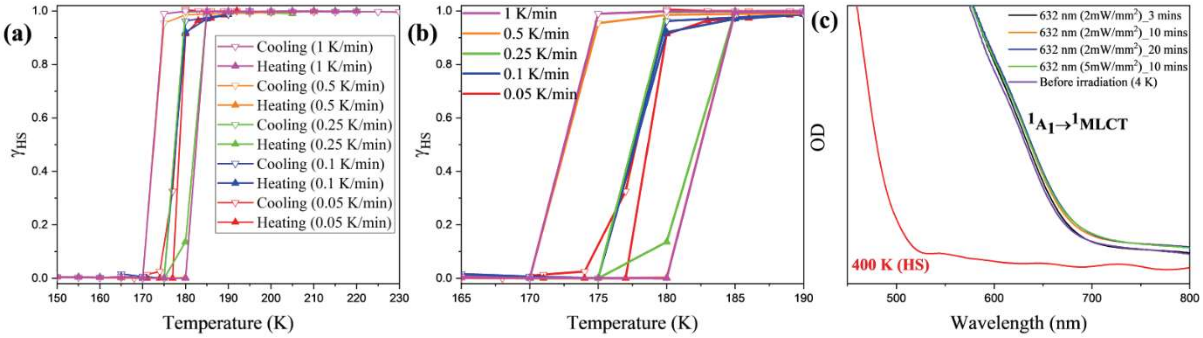

Figure 5. (a) Temperature-dependent plots of the normalized high-spin fraction (γ_{HS}) for dehydrated $[Fe(bppsipr)_2](BF_4)_2$ single crystal measured between 170 K and 195 K at different scan rates: 1 K/min (pink), 0.5 K/min (orange), 0.25 K/min (green), 0.1 K/min (blue), and 0.05 K/min (red). **(b)** Enlarged view of the spin-transition region highlighting the scan-rate dependence. **(c)** Optical absorption spectra of the dehydrated sample at 4 K: before irradiation (violet), and after continuous irradiation with a 632 nm He–Ne laser (2 mW/mm^2) for 3 minutes (black), 10 minutes (orange), and 20 minutes (blue). The red spectrum indicates the 400 K thermal absorption after complete dehydration. The green spectrum corresponds to 10 minutes of irradiation at an increased laser power of 5 mW/mm^2.

Figures 4a and 4b display the thermal spin-transition behavior of the hydrated compound $[Fe(bppsipr)_2](BF_4)_2 \cdot H_2O$, while Figure 5a presents similar data for the dehydrated form $[Fe(bppsipr)_2](BF_4)_2$. These plots are derived from the corresponding single-crystal UV-Vis absorption measurements shown in Figures 1 and 2, respectively. The data are represented as the high-spin fraction (γHS) versus temperature for various temperature sweep rates: 1 K/min (red), 0.5 K/min (blue), 0.25 K/min (green), 0.1 K/min (pink), and 0.05 K/min (violet) for the hydrated crystal (Figures 4a–b), and 1 K/min (pink), 0.5 K/min (orange), 0.25 K/min (green) 0.1 K/min (blue), and 0.05 K/min (red) for the dehydrated sample (Figure 5a). The high-spin fraction (γ_{HS}) is calculated using the following normalization equation:[37]

$$\gamma_{\mathrm{HS}} = \frac{OD_{\mathrm{LS}}^{\max} - OD(T)}{OD_{\mathrm{LS}}^{\max} - OD_{\mathrm{HS}}^{\max}} \qquad (1)$$

where $OD(T)$ is the temperature-dependent optical density in the 635–640 nm range, while OD_{LS}^{max} *and* OD_{HS}^{max} correspond to the maximum and minimum reference absorbance values associated with the pure LS and HS states, respectively. The normalization condition $\gamma_{HS} + \gamma_{LS} = 1$ ensures a straightforward and quantitative description of the spin-state population across the temperature range. To improve accuracy, a baseline correction was applied by subtracting the absorbance in the flat, featureless region between 750–755 nm from the signal in the 635–640 nm range. This correction minimizes background contributions and enhances the precision of the γ_{HS} determination.

As shown in Figure 4a, the thermal spin transition of the hydrated single crystal $[Fe(bppsipr)_2](BF_4)_2 \cdot H_2O$ occurs between 190 K (HS state) and 170 K (LS state). To highlight the influence of scan rate, Figure 4b provides a magnified view of the transition region (170-190 K). The spin transition is abrupt and complete at all scan rates, exhibiting thermal hysteresis with widths of 6 K at 1 K/min, 5 K at 0.5, 0.25, and 0.1 K/min, and 3 K at 0.05 K/min. Table 1 summarizes the spin-transition temperatures ($T_{½}\downarrow$ for cooling and $T_{½}\uparrow$ for heating), hysteresis widths, and average transition temperatures for hydrated, dehydrated, and dehydrated–annealed single crystals.

The thermal hysteresis is largely attributed to kinetic factors and is governed by the interplay between the activation barrier for spin-state relaxation, the strength of cooperative interactions, the temperature sweep rate, and the relaxation dynamics near the transition region.[57] These parameters are often modulated by structural changes such as phase transitions, crystallographic rearrangements, or modifications in crystal packing.[58] In this context, Brooker et al. have reviewed a wide range of Fe(II) complexes, illustrating how activation energy, scan rate, hysteresis width, transition sharpness, and loop temperature are interdependent and collectively influence the nature of the SCO transition.[57-59]

Notably, in the present study, the average transition temperature ($T^{½}_{average} = (T_{½}{\downarrow} + T_{½}{\uparrow}) / 2$) remains nearly constant across all scan rates for the hydrated form, despite minor variations in $T_{½}{\downarrow}$ and $T_{½}{\uparrow}$. Interesting, this is significantly lower than previously reported values from SQUID magnetometry, which were also invariant with scan rate but occurred at ca 30 K higher temperature ($T_{½}{\downarrow}$ = 212 K, $T_{½}{\uparrow}$ = 214 K at 0.4 K/min[35] and $T_{½}{\downarrow}$ = 210 K, $T_{½}{\uparrow}$ = 214 K at 5 K/min[34]). The consistent $T^{½}_{average}$ across scan rates suggests minimal variation in the zero-point energy gap (ΔE^0_{HL}), indicating stable local crystal fields between the HS and LS states. The slight scan rate dependence in $T_{½}{\downarrow}$ and $T_{½}{\uparrow}$ reflects a low activation barrier for thermal spin-state relaxation and a relatively high loop region temperature, resulting in fast spin kinetics and reduced sensitivity to scan rate. This also implies minimal structural rearrangement or crystal packing or defect formation between cooling and heating cycles. Such slight variation in hysteresis width with scan rate in the hydrated phase suggests subtle differences in cooperative interactions, which stem from the interplay of elastic and magnetic exchange interactions with varying degree of electron-phonon and spin-phonon coupling.

Traditionally, cooperativity has been linked to elastic interactions arising from volume changes between LS and HS states, involving both short- and long-range lattice forces.[60] However, density functional theory (DFT) studies have revealed that magnetic superexchange interactions, transmitted through bridging ligands, also play a significant role.[9,61,62] Building on this understanding, Banerjee et al. used Monte Carlo simulations with a model Hamiltonian incorporating spin-phonon coupling, magnetic superexchange, and elastic interactions.[9,61] Their results demonstrate that the dominant mechanism-whether elastic or magnetic-depends on the specific nature of spin-phonon coupling. This underscores that the origin of cooperativity in SCO systems is inherently material-dependent and cannot be attributed to a single universal mechanism.

During the HS → LS transition (cooling), elastic interactions dominate due to volume contraction and associated elastic energy gain, while magnetic energy is lost. This loss introduces an additional energy barrier in the cooling path, resulting in asymmetric behavior where the transition temperature on cooling ($T_{½}\downarrow$) is lower than on heating ($T_{½}\uparrow$), thereby broadening the hysteresis.[9,62] Conversely, during LS → HS transition (heating), magnetic superexchange interactions become significant due to the gain in magnetic energy and a simultaneous loss in elastic energy. Elastic interactions are primarily driven by volume changes between spin states and manifest as slow nucleation of like-spin domains followed by accelerated domain growth via both short- and long-range components. Magnetic interactions arise from spin-sublattice couplings between LS-LS, HS-HS, and HS-LS centers.[62]

The discrepancy between the spin transition temperatures observed in optical versus magnetic measurements can be attributed to two key factors:

(a) *Measurement Sensitivity*: The current study employs single-crystal optical absorption spectroscopy, which is highly sensitive to sample quality, size, and lattice imperfections (e.g., microcracks, defects). These factors influence spin relaxation kinetics and ΔE^0_{HL} (i.e., spin state energetics) through domain formation, clustering, and communication, effectively stabilizing the HS state by reducing the ΔE^0_{HL}. In contrast, previous magnetometry data were collected from bulk powder samples, providing ensemble-averaged behavior.

(b) *Solvation and Environmental Effects*: In this optical study, kinetic stabilization of the HS state during cooling may be facilitated by subtle shifts in lattice water molecules near the Fe(II) centers. Though the water molecule lies beyond coordination distance, they can modulate local packing, impose negative chemical pressure, and influence spin-state energetics. The vacuum conditions inside the optical cryostat may promote such rearrangements, favoring HS stabilization and altering transition behavior.

Similar to the hydrated phase, the dehydrated compound $[Fe(bppsipr)_2](BF_4)_2$ (Figure 5a) also exhibits an abrupt spin transition with a clear temperature scan rate dependence in thermal hysteresis width (see Figure 5b). Notably, while the average transition temperature ($T^{½}_{average}$) remains largely unchanged compared to the hydrated analogue, the cooling branch ($T_{½}\downarrow$) shifts to lower temperatures at faster scan rates (1 K/min and 0.5 K/min), whereas the heating branch ($T_{½}\uparrow$) remains nearly constant across all scan rates. At 0.25 K/min, the transition behavior closely mirrors that of the hydrated phase, with comparable $T_{½}\downarrow$, $T_{½}\uparrow$, and hysteresis width. However, at slower rates (0.1 K/min and 0.05 K/min), the hysteresis disappears, indicating a fully reversible spin transition. The similarity in $T^{½}_{average}$ across scan rates and between hydrated and dehydrated forms reflects minimal fluctuation in the average ΔE^0_{HL} and effective crystal field around the Fe(II) centers. However, the pronounced scan rate-dependent variation in hysteresis width for the dehydrated form-particularly the decrease in $T_{½}\downarrow$ at faster rates points to significant kinetic and structural differences upon dehydration.

Two main factors account for this behavior: (a) *Increased Activation Barrier After Dehydration*: Removal of the lattice water molecule increases the activation energy for spin-state relaxation, especially when the loop region temperature is relatively low. This leads to a pronounced hysteresis at higher scan rates that gradually narrows and eventually vanishes at slower rates (see Table 1). Despite no crystallographic phase change (the space group remains monoclinic $P21/c$), dehydration induces subtle but significant alterations in structural parameters-such as geometric distortion, crystal packing, intermolecular interactions (e.g., hydrogen bonding or dipolar contacts), and lattice rigidity-that contribute to a higher energy barrier and slower thermal kinetics.

(b) *Altered Cooperative Interactions:* In the dehydrated phase, the balance between elastic and magnetic interactions during cooling and heating cycles differs from that of the hydrated form. During the HS → LS transition (cooling), insufficient time at faster scan rates prevents the system from fully adjusting to the loss of magnetic exchange energy, introducing an additional energy barrier that shifts $T_{½}\downarrow$ to lower temperatures and broadens the hysteresis. This behavior reflects the persistence of the HS state due to strong magnetic memory. As the scan rate decreases, the system gains more time to adapt, allowing gradual compensation of magnetic loss with elastic energy gain. At the slowest rates, the system fully accommodates these changes, eliminating memory effects and leading to a sharp, reversible transition without hysteresis. In contrast, the LS → HS transition (heating) shows little to no scan rate dependence. This asymmetry suggests that LS states lack significant memory effects; the gain in magnetic exchange energy during heating is less influenced by prior thermal history and proceeds similarly across scan rates. Overall, these observations highlight how dehydration alters the balance of kinetic and cooperative effects, resulting in a stronger dependence on scan rate and the emergence (or loss) of thermal hysteresis in spin-crossover behavior.

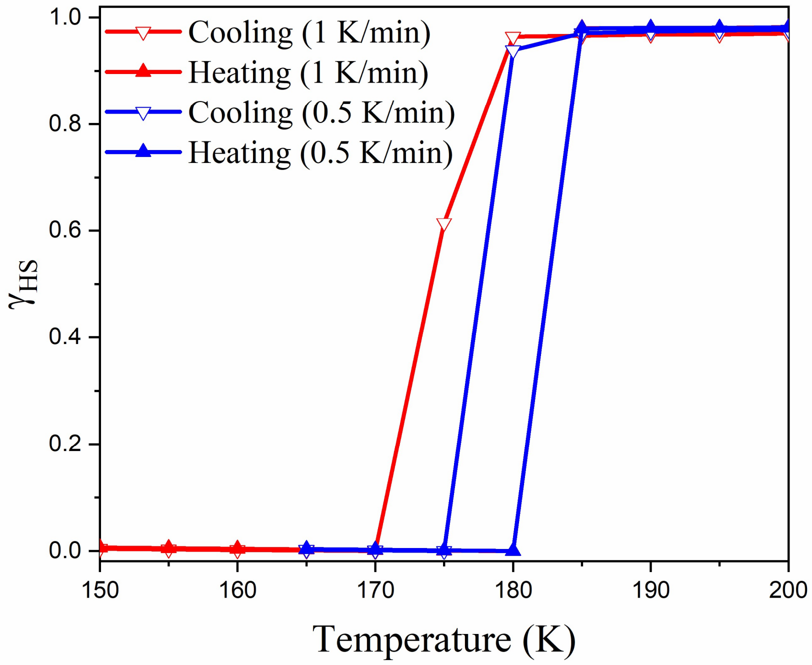

Figure 6. Temperature-dependent plots of the normalized high-spin fraction (γHS) for the annealed dehydrated [Fe(bppsipr)$_2$](BF$_4$)$_2$ single crystal, recorded at scan rates of 1 K/min (red) and 0.5 K/min (blue).

To explore the influence of thermal history on spin-state switching, temperature sweep rate-dependent measurements are performed on the dehydrated single crystal following a thermal annealing treatment at 350 K for 30 minutes. This annealing step is designed to relieve structural distortions, microcracks, lattice imperfections, and local disorder that may have developed during repeated thermal cycling. By restoring a more ordered crystalline framework, annealing can influence cooperative interactions and thereby modulate thermal hysteresis behavior. Post-annealing, measurements are conducted at two scan rates: 1 K/min and 0.5 K/min. After each thermal cycle, the single crystal was re-annealed to maintain consistent conditions. At 1 K/min (Figure 6), the spin transition remained qualitatively similar to the unannealed dehydrated sample but exhibited a reduced hysteresis width-from 10 K to 8 K primarily due to a shift in the cooling branch transition temperature ($T_{1/2}\downarrow$) to a higher value, while the heating branch ($T_{1/2}\uparrow$) remained unchanged. Further annealing and reducing the scan rate to 0.5 K/min led to an additional upward shift in $T_{1/2}\downarrow$, narrowing the hysteresis width to 5 K (Figure 6). This behavior suggests that progressive annealing improves the system's ability to accommodate the loss of magnetic exchange interactions and associated energy during the HS → LS transition. The reduction in lattice defects and local disorder enhances the formation and growth of LS domains through elastic interactions-both short- and long-range-while simultaneously weakening the memory effect that stabilizes the HS state. Importantly, the consistent $T_{1/2}\uparrow$ values across different scan rates and thermal histories confirm that the LS → HS transition during heating is largely scan rate-independent. This behavior indicates that the magnetic energy gain associated with the LS → HS transition dominates the process and is relatively insensitive to sample history, crystal quality, or microstructural variations.

Table 1. Summary of spin transition temperatures ($T_{1/2}\downarrow$, $T_{1/2}\uparrow$ and $T^{1/2}_{average}$) and hysteresis widths for hydrated and dehydrated forms of $[Fe(bppsipr)_2](BF_4)_2$, including data for annealed dehydrated sample. Measurements are performed at various temperature scan rates to assess the influence of lattice hydration and thermal treatment on the spin state switching behavior.

	$\Delta T_{1/2}$ (Hysteresis width)	**Temperature sweep rate**	**$T^{1/2}_{average}$**
$[Fe(bppsipr)_2](BF_4)_2\cdot H_2O$ (Hydrated)	6 K (177 K to 183 K)	1 K/min	180 K
	5 K (177 K to 182 K)	0.5 K/min	179.5 K
	5 K (177 K to 182 K)	0.25 K/min	179.5 K
	5 K (177 K to 182 K)	0.1 K/min	179.5 K
	3 K (178 K to 181 K)	0.05 K/min	179.5 K

$[Fe(bppsipr)_2](BF_4)_2$ (Dehydrated)	10 K (172 K to 182 K)	1 K/min	177 K
	10 K (172 K to 182 K)	0.5 K/min	177 K
	4 K (178 K to 182 K)	0.25 K/min	180 K
	No hysteresis (177 K)	0.1 K/min	177 K
	No hysteresis (177 K)	0.05 K/min	177 K
$[Fe(bppsipr)_2](BF_4)_2$ (Dehydrated, annealed)	8 K (174 K to 182 K)	1 K/min	178 K
	5 K (177 K to 182 K)	0.5 K/min	179.5 K

LIESST, T(LIESST) and Reverse-LIESST

At 4 K, the hydrated complex $[Fe(bppsipr)_2](BF_4)_2 \cdot H_2O$ is irradiated with a 632 nm continuous-wave (cw) HeNe laser (power density ~2 mW/mm^2) for five minutes. This exposure completely bleached the characteristic LS ^{1}MLCT absorption band and led to the emergence of a blue-shifted ^{5}MLCT band corresponding to the HS state, confirming an efficient photoinduced spinstate conversion via the LIESST effect (see dark brown spectra in Figure 4c). The high quantum efficiency of this process enabled full conversion to the metastable HS state at low temperature. The resulting photoinduced spectrum closely matches that of the thermally generated HS state at 300 K, validating complete transformation. At 4 K, thermal relaxation from the photoinduced HS to the LS ground state is extremely slow, effectively trapping the system in the metastable HS state for extended durations. This kinetic stability allows detailed exploration of the photoinduced dynamics, without noticeable changes in HS population over time. The temperature-dependent spectral evolution of the photo-generated HS state during slow heating (0.3 K/min) is shown in Figure 4c. The initial spectrum at 4 K (dark brown) remains unchanged over a wide temperature range, indicating a prolonged incubation phase. A sudden red shift at higher temperatures signals the onset of HS → LS relaxation, indicating a high T(LIESST) value.

After normalization, the corresponding plot of high-spin fraction (γHS) versus temperature is shown in Figure 4a. Upon photoexcitation, γHS rapidly reaches 1 (indicated by a red arrow) confirming full HS-state population. The HS fraction remains nearly constant up to ~ 60 K, beyond which a sharp drop defines T(LIESST) at 78 K, consistent with previously reported values (~ 81 K), and among the highest recorded for 1-bpp-based Fe(II) systems. A minor dip near 35 K, likely due to slight changes in spectral shape, results in a small fluctuation in the normalized data (Figure 4a and 4c), but remains within the experimental margin of error. Following irradiation, a distinct baseline shift appears in the absorption spectra-absent during thermal cycling. Since earlier studies have ruled out crystallographic phase transitions upon light exposure, this shift is attributed to increased diffuse scattering from photoinduced domain formation.[35] These domains, having dimensions on the order of the incident light's wavelength, likely result from subtle lattice rearrangements involving water molecules, counterions, and other dipolar entities. This behavior indicates a structural difference between the photoinduced HS (LIESST) state, the thermal HS state, and the ground LS state. Such differences likely arise from variations in crystal packing, local lattice strain, or the formation of microcracks during photoexcitation. At low temperatures, weak interference-like patterns are also observed in the photo-generated HS spectra. These are most likely caused by: (a) diffuse scattering from randomly formed HS domains or clusters, and (b) laser-induced mechanical stress leading to microcracks or air gaps, which in turn cause multiple reflections. These features disappear upon heating, suggesting that the crystal undergoes annealing and returns to a more uniform structural state.

The low-temperature region of the T(LIESST) curve (below ~ 60 K) defines an "incubation zone," where the photoinduced high-spin (HS) state remains effectively trapped due to a high thermal activation barrier and slow structural reorganization. In this regime, the system is thought to prepare for a cooperative, self-accelerated HS → LS relaxation process that initiates above ~ 60 K. Beyond this threshold, spin-state relaxation proceeds rapidly, driven by both short- and long-range electron-phonon interactions. These processes are accompanied by significant volume changes in the metal coordination sphere and crystal packing rearrangement. As the temperature increases further, the relaxation mechanism transitions into a thermally activated, over-barrier regime, characteristic of classical kinetics. This distinctive T(LIESST) behavior motivated further investigation into the temperature-dependent relaxation dynamics of the photoinduced HS state near the transition region in the hydrated single crystal, as detailed in the following section.

In contrast, LIESST experiments on the dehydrated compound $[Fe(bppsipr)_2](BF_4)_2$ do not reveal any measurable spectral changes (Figure 5c). This absence of a detectable photoresponse suggests that the photoinduced HS state relaxes too quickly to be observed with our instrumentation, which requires the metastable state to persist for at least a few minutes. This finding stands in stark contrast to the hydrated analogue, where the photoinduced HS state is stable and observable up to ~ 60 K. The lack of a long-lived HS state in the dehydrated compound likely stems from structural reorganization/rearrangement upon photoexcitation including the formation of laser-induced crystal defects or micro-cracks. These result enhanced crystal field strength, increased lattice rigidity, and changes involving cations, anions, or other dipolar species, all of which collectively favor stabilization of the LS state. Thus, such changes upon photoexcitation, significantly increase ΔE^0_{HL}, shifting the energy balance toward the LS configuration. The theoretical model study within the framework of mechanoelastic model discussed below provides a qualitative insight of the hydrated phases and accordingly highlights the photoinduced spin relaxation behavior of the hydrated crystal. However, the exact microscopic origin remains unclear and will require further investigation through advanced techniques such as time-resolved, temperature-dependent photocrystallography and time-resolved optical spectroscopy.

To further assess the bidirectional light-switching capability of the hydrated crystal, we perform a reverse-LIESST experiment at 4 K. Following initial excitation into the metastable HS state using a 632 nm cw HeNe laser (~ 2 mW/mm^2), the sample is irradiated with 830 nm light from a DPSS laser (~ 30 mW/mm^2) for 72 minutes. This reverse process-well documented in other Fe(II)-based spin-crossover systems-facilitates re-population of the LS ground state and is of significant interest for light-driven bistability and optical memory applications.[12,16,17] As expected, the reverse-LIESST process shows much lower quantum efficiency (~ 10%) compared to the forward LIESST, consistent with literature reports[12,16,17] Figure 4d shows the spectral evolution during this process: the photoinduced HS spectrum (dark brown) shifts slightly red upon reverse irradiation (pink), indicating partial LS recovery. However, due to strong LS absorption near this spectral region, accurately quantifying the converted LS fraction is challenging. Subsequent thermal relaxation (at 0.3 K/min) fully restored the LS ground state, with the resulting spectrum matching that from the thermal cycling experiment. Notably, the absence of a baseline shift during this evolution indicates no significant diffuse scattering, suggesting a lack of domain structures comparable in size to the incident light wavelength. However, such behavior may depend on the specific system, crystal quality, or experimental setup and should not be universally assumed.[63] As with the T(LIESST) transition, this spectral evolution provides valuable insight into thermal relaxation kinetics. Nonetheless, the reverse-LIESST process remains markedly less efficient in the hydrated compound, especially when compared to benchmark systems like $[Fe(ptz)_6]^{2+}$. This inefficiency is attributed to the presence of a low-lying ^{1}MLCT band in the LS state, which energetically suppresses the reverse-LIESST pathway (i.e., $^5T_2 \rightarrow {}^5E \rightarrow {}^3T_1 \rightarrow {}^1A_1$).[46] In summary, the hydrated compound exhibits highly efficient LIESST behavior and modest reverse-LIESST response. These observations reflect the delicate balance between excited-state energetics and the competing photophysical pathways that govern light-induced spin-state switching. The results emphasize the critical role of fine-tuned molecular and crystal engineering for optimizing bistable SCO materials for optical and memory-based applications.

Photoinduced HS → LS relaxation

To gain deeper insight into the relaxation dynamics of the photoinduced metastable HS state, time-resolved optical measurements are performed on the hydrated single crystal. Figure 7 presents high-resolution spectral evolution during the HS → LS relaxation process, monitored across a temperature range of 50 - 75 K. The experimental procedure begins with photoexcitation of the crystal at 4 K using a 632 nm continuous-wave (cw) laser (5 minutes, ~2 mW/mm2) to generate the metastable HS state. The crystal is then rapidly heated to the target temperature and held isothermally while the absorption spectra are recorded as a function of time, capturing the relaxation of the HS state back to the LS ground state. This relaxation was tracked at five different temperatures: 50 K, 60 K, 65 K, 70 K, and 75 K, allowing for detailed analysis of the temperature-dependent kinetics. At each temperature, the evolution of the LS-associated 1MLCT shoulder band around 635 - 640 nm was monitored as a direct probe of the HS → LS transition. After each measurement cycle, the crystal was cooled back to 4 K, and the process was repeated to ensure experimental consistency.

At 50 K and 60 K, the spectral features remained largely unchanged over time, indicating that relaxation is extremely slow in this temperature range - consistent with a high activation barrier. In contrast, at 65 K, 70 K, and 75 K, significant spectral changes were observed, reflecting a faster decay of the metastable HS state and confirming thermally activated relaxation kinetics.

Alongside spectral evolution, a noticeable baseline shift appeared in the absorption spectra following photoexcitation, in line with the behavior observed in earlier LIESST experiments. This baseline shift is likely due to increased diffuse scattering caused by the formation of randomly distributed LS domains and accompanying lattice reorganization. Additionally, interference-like patterns were observed post-irradiation, attributed to laser-induced mechanical stress leading to the development of microcracks and air gaps within the crystal. These defects create multiple internal reflections, giving rise to interference fringes in the spectra. Crucially, both the baseline shifts and interference patterns disappeared progressively as the system relaxed back to the LS state, indicating a self-annealing property of the hydrated crystal. This suggests that the lattice can recover from photoinduced structural perturbations during thermal relaxation, restoring its structural homogeneity after each cycle.

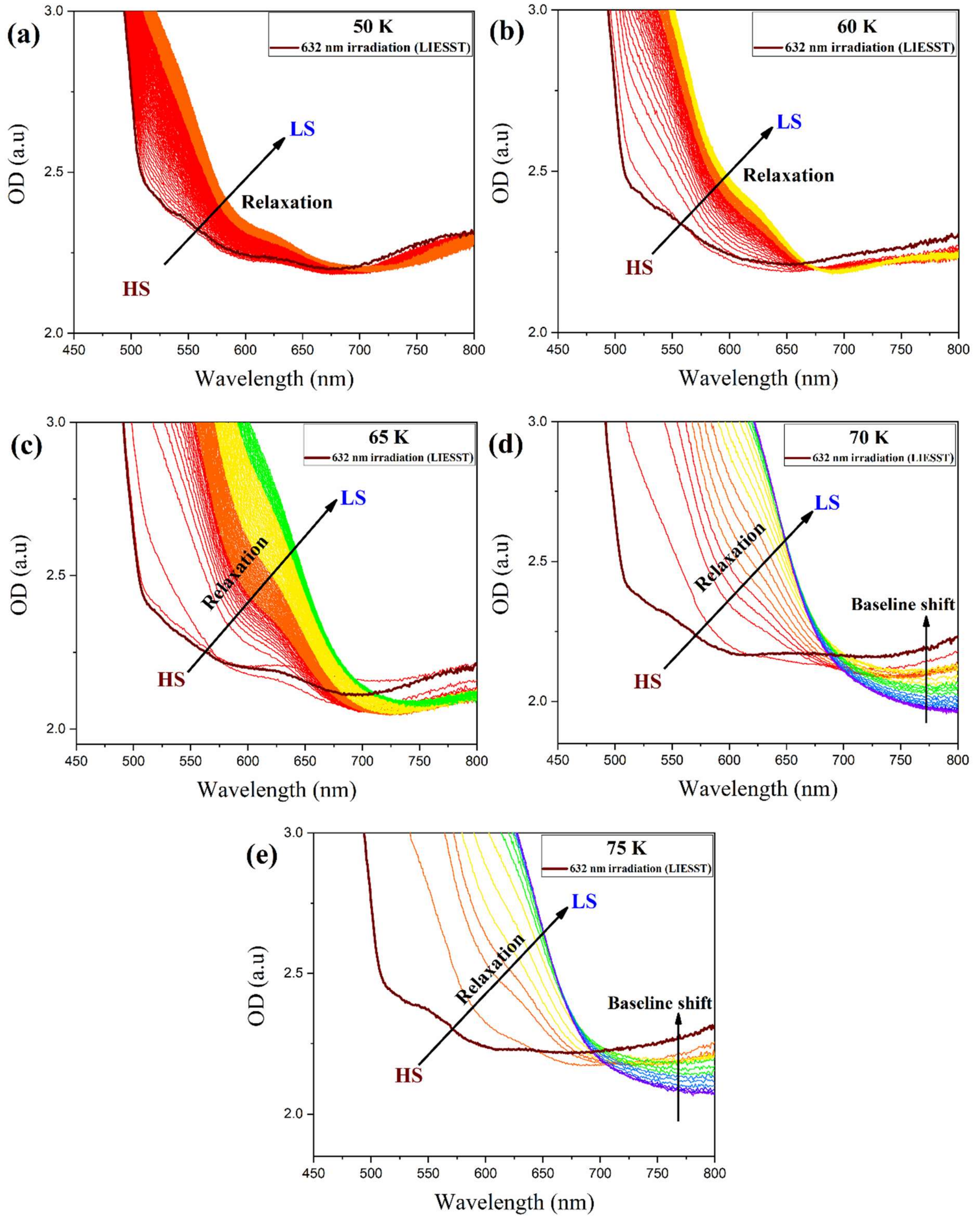

Figure 7. Time-resolved high-resolution single-crystal UV‑Vis absorption spectra of hydrated [Fe(bppsipr)$_2$](BF$_4$)$_2$.H$_2$O, recorded during the relaxation of the photoinduced HS state to the LS state at selected temperatures (50 K, 60 K, 65 K, 70 K, and 75 K). The measurements follow LIESST using 632 nm light at a nominal power density of 2 mW/mm^2. The black angular arrow

indicates the direction of the HS → LS relaxation, while the black vertical arrow highlights the baseline shift observed during the relaxation process.

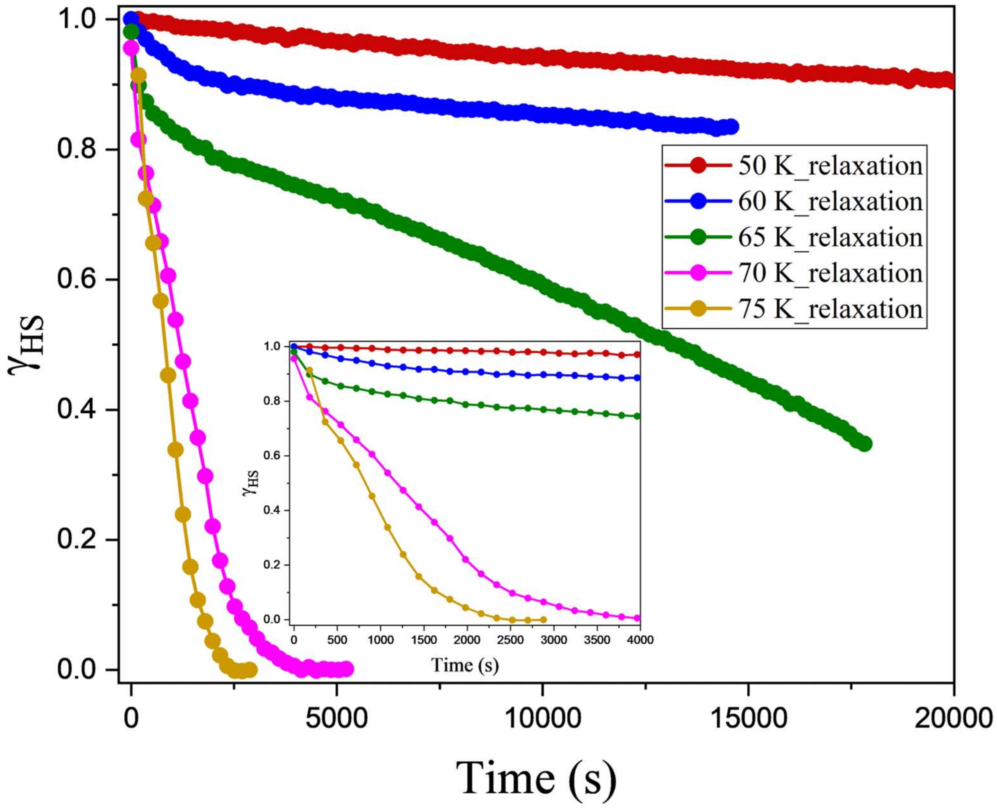

Figure 8. Photoinduced HS to LS relaxation behavior of hydrated [Fe(bppsipr)$_2$](BF$_4$)$_2$.H$_2$O single crystal at various target temperatures, extracted directly from the time-resolved high-resolution single-crystal UV-Vis absorption spectra shown in Figure 7. Inset: Magnified view of the relaxation behavior in shorter time scales.

Figure 8 presents the time-resolved relaxation behavior of the hydrated single crystal during the HS to LS transition, monitored at five different temperatures: 50 K (red), 60 K (blue), 65 K (green), 70 K (magenta), and 75 K (dark yellow). These target temperatures are selected based on the thermal behavior observed in the T(LIESST) curve, particularly focusing on the temperature window where dynamic relaxation becomes significant. The relaxation profiles shown are derived from the time-dependent UV-Vis absorption spectra in Figure 7, recorded at three-minute intervals after LIESST excitation at 4 K. The normalized high-spin fraction (γ_{HS}) is calculated using Equation 1, applying the condition $\gamma_{HS} + \gamma_{LS} = 1$. Spectra recorded before and after light irradiation at 4 K are used as reference states for the pure LS and HS configurations, respectively.

The shapes of the γ_{HS} vs. time curves reveal key insights into the underlying relaxation mechanisms and cooperative dynamics:

- At 50 K, the γ_{HS} remains nearly constant over the entire measurement period, indicating that the photoinduced HS state is effectively trapped due to a high thermal activation barrier. LS nucleation is strongly hindered by slow structural reorganization, leading to a prolonged incubation period with negligible relaxation.

- At 60 K, a slow and minor single-exponential decay in γ_{HS} is observed, followed by a plateau, suggesting a pseudo steady-state. This behavior implies that ~10% of LS domains form stochastically within the HS lattice without initiating long-range cooperative conversion. The thermal energy at this temperature appears sufficient to trigger localized HS → LS relaxation, but not enough to overcome the cooperative threshold for extended domain growth. Alternatively, it is plausible that the system stabilizes in a persistent LS:HS = 10:90 configuration, where further relaxation is inhibited by the remaining high energy barrier.

- At higher temperatures (65 K, 70 K, and 75 K), the relaxation curves exhibit a distinct two-step character (inset of Figure 8): (a) The initial phase follows a single-exponential decay, reflecting random nucleation of LS domains - approximately 17% at 65 K, 20% at 70 K, and 30% at 75 K in the HS lattice. (b) The second phase shows a sigmoidal progression, characteristic of cooperative domain growth. This suggests that once a critical concentration of LS sites is reached, collective lattice reorganization and domain-domain communication are activated, accelerating the HS → LS transition through a self-propagating mechanism.

This two-step behavior likely arises from structural changes or adjustments in crystal packing that occur during photoexcitation and subsequent thermal relaxation. These changes reduce elastic energy, facilitating non-random clustering of like-spin domains. Consequently, this modulates ΔE^0_{HL} and enhances relaxation kinetics by promoting long-range cooperativity and the emergence of spin-sublattice ordering (e.g., LS:HS = 17:83 at 65 K, 20:80 at 70 K, and 30:70 at 75 K, as illustrated in the inset of Figure 8 as magnified view). Such mixed relaxation kinetics-comprising both exponential and sigmoidal phases-have previously been observed, for example by Halcrow *et al.* in $[\mathrm{Fe(bppI)_2}](\mathrm{BF_4})_2$ (bppI= 4-iodo-2,6-di(pyrazol-1-yl)-pyridine).[64] The temperature-dependent HS → LS relaxation dynamics of the hydrated single crystal underscore the complex interplay between thermal activation barriers, elastic energy contributions, local structural changes, and cooperative interactions within the lattice.

Model

To gain deeper insight into the microscopic mechanisms and molecular-level structural changes underlying the cooperative photoinduced HS → LS relaxation-particularly those driven by structural rearrangements and modifications in crystal packing - a comprehensive mechanoelastic model is employed. This modified model effectively captures the complex relaxation behavior observed in the hydrated system. In this approach, the SCO material is represented as a network of spheres connected by springs. Each sphere corresponds to an individual SCO-active molecule, with its radius varying according to its spin state (HS or LS), while the springs symbolize the elastic interactions (or bonds) between neighboring molecules.

The model incorporates both global parameters such as temperature and crucial local environmental factors that influence spin-state switching. A central feature of the model is its ability to simulate molecular switching events as being governed by local pressure fluctuations acting on each SCO center. These local variations stem from changes in crystal packing, lattice distortions, dipolar interactions, and the formation of like-spin clusters. Particularly important is the inclusion of local mechanical stress generated by volume changes accompanying spin-state transitions, which serves as a key driving force in the relaxation dynamics. By accounting for these effects, the mechanoelastic model successfully reproduces a broad spectrum of experimental observations. These include: (a) Diverse relaxation dynamics across different length scales-from bulk crystals to nanoparticles,[65,66] (b) Variable shapes and widths of both thermal and light-induced hysteresis loops,[67,68] (c) Rapid spin-state relaxation phenomena.49 Overall, this model provides a powerful framework for understanding the interplay between mechanical, structural, and cooperative effects in spin-crossover materials, offering valuable insights into the mechanisms governing their responsive behavior under light and thermal stimuli.

The model uses a two-step approach: in a first step, a set of two transition probabilities ‑ from LS to HS and from HS to LS - are computed for each molecule. The probabilities (eq. 1) depend on material parameters, like ΔH and ΔS which are the enthalpy and the entropy variations during the switch and E_a the activation energy, on global parameters, like temperature T, as well as on local pressure $p^{(\mathrm{i})}$ that acts on the i-th molecule through the connected springs.

$$\begin{cases} P_{LS\rightarrow HS}^{(i)} = \dfrac{1}{\tau}\exp\left(-\dfrac{\Delta H - T\Delta S}{2k_B T}\right)\exp\left(-\dfrac{E_a - kp^{(i)}}{k_B T}\right) \\ P_{HS\rightarrow LS}^{(i)} = \dfrac{1}{\tau}\exp\left(\dfrac{\Delta H - T\Delta S}{2k_B T}\right)\exp\left(-\dfrac{E_a + kp^{(i)}}{k_B T}\right) \end{cases} \quad (1)$$

k scales the effect of the local pressure relative to the activation energy and t is used to normalize the probabilities to values smaller than 1. The first step ends with a typical Monte Carlo Arrhenius procedure, by comparing the values of the probabilities with random numbers selected from a uniform random number distribution between 0 and 1 and deciding the new spin state of each molecule in the system. In a second step, the radius of each sphere is updated according to its spin state, as resulted from the previous step, and then a system of classical differential equations characterizing the motion of each molecule (eq. 2) is solved to find their new equilibrium position.

$$\begin{cases} m\dfrac{d^2x_i}{dt^2} = F_{xi} - \mu\dfrac{dx_i}{dt} \\ m\dfrac{d^2y_i}{dt^2} = F_{yi} - \mu\dfrac{dy_i}{dt} \end{cases} \qquad (2)$$

Where m is the inertial mass of a molecule, (x_i, y_i) and (F_{xi}, F_{yi}) are the coordinates set and the force components acting on the i-th molecule and μ is a dissipation parameter. The above steps are repeated in order to study the evolution of the system either in time or when the temperature changes.

The mechanoelastic model was enhanced to study the hydrated samples discussed in this paper by considering that the presence of water molecules acts as a supplementary pressure term, thus $p^{(i)}$ (in eq. 1) becomes $p^{(i)} = p^{(i)}_{elastic} + p^{(i)}_{water}$ where $p^{(i)}_{elastic}$ represents the sum of forces acting on the i-th molecule through springs, similar to previous versions of the model,[65-68] while $p^{(i)}_{water}$ is a new term, constant in value for a certain site in the system as well as for all the simulation runs involving hydrated samples, but with values randomly chosen from a narrow normal distribution centered at zero, designed to account all kinds of inhomogeneities in the system. This mechanoelastic framework is applied to successfully simulate all the experimental photoinduced cooperative HS → LS relaxation curves of the hydrated crystal shown in Figure 8.

In the context of relaxation studies, it is important to note that the photoinduced HS state generated via LIESST in the present hydrated system exhibits Jahn‑Teller distortion. This distortion arises from angular deviations-particularly in the trans and dihedral angles-within the coordination sphere, due to the orbital degeneracy inherent in the HS state. To more accurately capture this structural distortion in the mechanoelastic model, an additional term is introduced into the local pressure expression. This third term explicitly accounts for the angular distortion associated with the Jahn‑Teller effect, complementing the existing contributions from lattice water and volume changes during the spin-state transition:

$$p^{(i)} = p^{(i)}_{elastic} + p^{(i)}_{water} + p^{(i)}_{distortion} .$$

The system is initially driven to a fully high-spin (HS) state, simulating complete photoexcitation. It is then allowed to relax under experimental conditions by setting the environmental temperature to match the measured values. The relaxation dynamics are modeled using the mean field value of the distribution of the distortion pressure term as fit parameter, with the corresponding parameter values summarized in Table 2 for different temperatures:

Table 2. The summary of mean values of the distribution of distortion and the corresponding dispersion at different experimental relaxation temperatures.

Temperature	Distortion term distribution	
	Mean value	Dispersion
50 K	60.0	1.0
60 K	57.0	1.0

65 K	47	1.0
70 K	30	1.0
75 K	21	1.0

Collectively, these terms effectively reproduce the cooperative relaxation dynamics of the hydrated crystal across all experimental temperatures (Figure 9). The model captures the underlying microscopic mechanism, which involves nucleation and growth of like-spin domains and domain-domain interactions that modulate ΔE^0_{HL} during the relaxation process.

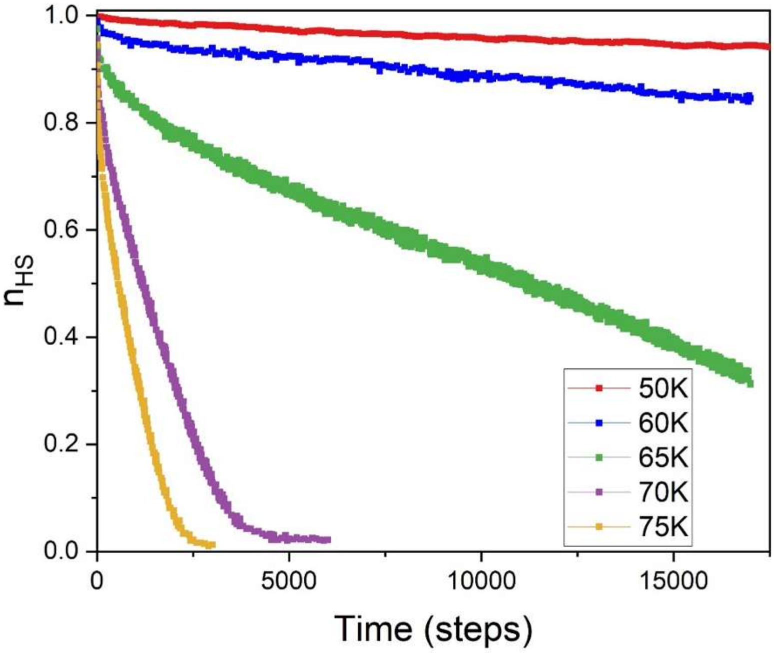

Figure 9. Simulated photoinduced high-spin (HS) to low-spin (LS) relaxation curves using the mechanoelastic model framework.

In summary, the mechanoelastic model, by incorporating local molecular effects and the influence of hydration, provides a robust and comprehensive framework for accurately describing the cooperative spin-state relaxation observed experimentally.

Conclusions

Using high-resolution single-crystal UV‑Vis absorption spectroscopy, this study provides a rare and detailed picture of spin-state switching, enabling direct tracking of MLCT band evolution under controlled thermal scan rates. By extracting $\gamma_{HS}(T)$, we uncovered distinct differences in the SCO dynamics of hydrated, dehydrated, and thermally annealed crystals. A key new observation is that lattice hydration dramatically governs the cooperativity and kinetics of the transition. The hydrated crystal shows a sharp, complete, and nearly scan-rate-independent transition with narrow hysteresis, whereas dehydration introduces pronounced scan-rate dependence, broader hysteresis, and enhanced kinetic hindrance. Thermal annealing partially restores structural order, narrowing the hysteresis and shifting cooling transition ($T_{½}\downarrow$) upward while leaving the heating transition ($T_{½}\uparrow$) largely unchanged—demonstrating that cooling hysteresis is more sensitive to kinetic barriers and elastic reorganization, while heating remains dictated by magnetic energy gain and is robust to defects. Equally striking are the hydration-dependent differences in photoinduced switching. The hydrated crystal undergoes efficient LIESST at 4 K, yielding a metastable HS state stabilized up to ~60 K by strong cooperativity. In contrast, the dehydrated crystal shows no measurable LIESST, as rapid HS → LS relaxation prevents metastable buildup—highlighting the critical role of lattice water in tuning crystal field strength and mechanical flexibility. Reverse-LIESST in the hydrated phase achieves only partial LS recovery (~10%), limited by a low-lying 1MLCT state. Time- resolved optical studies further reveal a two-step HS → LS relaxation pathway in the hydrated system between 65–75 K: an initial exponential nucleation of LS centers followed by cooperative sigmoidal domain growth. Below 60 K, relaxation is kinetically arrested, freezing a metastable HS-rich phase, whereas above this threshold, critical LS domain densities trigger self-propagating lattice transformation. To rationalize these behaviors, we extended a mechanoelastic model by incorporating a hydration-dependent pressure term that captures local stress inhomogeneity. Monte Carlo simulations reproduced the observed relaxation dynamics with high fidelity, confirming that domain nucleation, elastic coupling, and local structural rearrangements are central to cooperative SCO relaxation. Overall, our results establish hydration state and thermal history as decisive parameters in governing spin-crossover cooperativity, hysteresis, and photo-switchability. Beyond providing fundamental insights into the interplay of elastic stresses, domain dynamics, and light-induced processes, this work offers a clear blueprint for designing bistable SCO systems by systematically tuning the ligand backbone, counter-ion, and the reversible incorporation or removal of different solvent molecules. These factors enable precise control over hysteresis width, relaxation dynamics, and photoresponse - key characteristics required for developing optical memory, sensing, and molecular switching applications.

Author Contribution

CD conducted all structural and photophysical characterizations, analyzed the data, and drafted the manuscript. MAH was responsible for the synthesis and single-crystal growth. DC and LS carried out the theoretical modeling. The manuscript was conceptualized, supervised, and guided throughout by PC. All authors contributed to the organization, editing, and finalization of the manuscript. PC performed the final review and approval of the manuscript. All authors have read and approved the final version for publication.

Acknowledgements

P.C. sincerely acknowledges financial support from the SERB Core Research Grant (Grant No. CRG/2023/003032). C.D. acknowledges the research fellowship support from IIT Kharagpur.

Data Availability

The data supporting the findings of this study are provided in the Supplementary Information. Additional data are available from the corresponding author upon reasonable request.

Conflict of Interests

All authors declare no conflicts of interest.

References

1 J.-F. Létard, P. Guionneau and L. Goux-Capes, in *Spin Crossover in Transition Metal Compounds III*, eds. P. Gütlich and H. A. Goodwin, Springer, Berlin, Heidelberg, 2004, pp. 221–249.

2 J. Linares, E. Codjovi and Y. Garcia, *Sensors*, 2012, **12**, 4479–4492.

3 C. Bartual-Murgui, A. Akou, C. Thibault, G. Molnár, C. Vieu, L. Salmon and A. Bousseksou, *J. Mater. Chem. C*, 2015, **3**, 1277–1285.

4 A. Tsukiashi, K. S. Min, H. Kitayama, H. Terasawa, S. Yoshinaga, M. Takeda, L. F. Lindoy and S. Hayami, *Sci. Rep.*, 2018, **8**, 14911.

5 R. N. Muller, L. Vander Elst and S. Laurent, *J. Am. Chem. Soc.*, 2003, **125**, 8405–8407.

6 P. Gütlich and H. A. Goodwin, in *Spin Crossover in Transition Metal Compounds I*, eds. P. Gütlich and H. A. Goodwin, Springer, Berlin, Heidelberg, 2004, pp. 1–47.

7 J. A. Real, A. B. Gaspar, V. Niel and M. C. Muñoz, *Coord. Chem. Rev.*, 2003, **236**, 121–141.

8 E. Collet and P. Guionneau, *C. R. Chimie*, 2018, **21**, 1133–1151.

9 H. Banerjee, S. Chakraborty and T. Saha-Dasgupta, *Inorganics*, 2017, **5**, 47.

10 S. Decurtins, P. Gütlich, C. P. Köhler, H. Spiering and A. Hauser, *Chem. Phys. Lett.*, 1984, **105**, 1–4.

11 Y.-S. Meng and T. Liu, *Acc. Chem. Res.*, 2019, **52**, 1369–1379.

12 A. Hauser, in *Spin Crossover in Transition Metal Compounds II*, eds. P. Gutlich and H. A. Goodwin, Springer, Berlin, Heidelberg, 2004, pp. 155–198.

13 A. Hauser, *Coord. Chem. Rev.*, 1991, **111**, 275–290.

14 A. Hauser, J. Jeftić, H. Romstedt, R. Hinek and H. Spiering, *Coord. Chem. Rev.*, 1999, **190–192**, 471–491.

15 G. Li, O. Stefanczyk, K. Kumar, L. Guerin, K. Okuzono, K. Tran, M. Seydi Kilic, K. Nakabayashi, K. Imoto, A. Namai, Y. Nakamura, S. Ranjan Maity, F. Renz, G. Chastanet and S. Ohkoshi, *Angew. Chem. Int. Ed.*, 2025, **64**, e202423095.

16 A. Hauser, *Chem. Phys. Lett.*, 1986, **124**, 543–548.

17 A. Hauser, *J. Chem. Phys.*, 1991, **94**, 2741–2748.

18 T. Charytanowicz, M. Heczko, K. Dziedzic-Kocurek, D. Pinkowicz, S. Ohkoshi, S. Chorazy and B. Sieklucka, *J. Mater. Chem. C*, 2025, **13**, 6745–6761.

19 J.-F. Letard, *J. Mater. Chem.*, 2006, **16**, 2550–2559.

20 G. Chastanet, C. Desplanches, C. Balde, P. Rosa, M. Marchivie, P. Guionneau, *Chem. Sq.* 2018, **2**, 2.

21 V. Garcia-Lopez, M. Palacios-Corella, S. Cardona-Serra, M. Clemente-Leon and E. Coronado, *Chem. Commun.*, 2019, **55**, 12227–12230.

22 M.-L. Boillot, S. Pillet, A. Tissot, E. Riviere, N. Claiser and C. Lecomte, *Inorg. Chem.*, 2009, **48**, 4729–4736.

23 M.-L. Boillot, J. Zarembowitch and A. Sour, in *Spin Crossover in Transition Metal Compounds II*, eds. P. Gutlich and H. A. Goodwin, Springer, Berlin, Heidelberg, 2004, pp. 261–276.

24 A. Tissot, M.-L. Boillot, S. Pillet, E. Codjovi, K. Boukheddaden and L. M. Lawson Daku, *J. Phys. Chem. C*, 2010, **114**, 21715–21722.

25 Y. Hasegawa, K. Takahashi, S. Kume and H. Nishihara, *Chem. Commun.*, 2011, **47**, 6846–6848.

26 K. Takahashi, Y. Hasegawa, R. Sakamoto, M. Nishikawa, S. Kume, E. Nishibori and H. Nishihara, *Inorg. Chem.*, 2012, **51**, 5188–5198.

27 Y. Hasegawa, R. Sakamoto, K. Takahashi and H. Nishihara, *Inorg. Chem.*, 2013, **52**, 1658–1665.

28 C.-C. Wu, J. Jung, P. K. Gantzel, P. Gutlich and D. N. Hendrickson, *Inorg. Chem.*, 1997, **36**, 5339–5347.

29 R. Diaz-Torres, G. Chastanet, E. Collet, E. Trzop, P. Harding and D. J. Harding, *Chem. Sci.*, 2023, **14**, 7185–7191.

30 A. R. Zuluaga, A. J. Brock, M. C. Pfrunder, W. Phonsri, K. S. Murray, P. Harding, A. S. Micallef, K. M. Mullen, J. K. Clegg, D. J. Harding and J. C. McMurtrie, *Chem. Mater.*, 2020, **32**, 10076–10083.

31 K. S. Kumar, B. Heinrich, S. Vela, E. Moreno-Pineda, C. Bailly and M. Ruben, *Dalton Trans.*, 2019, **48**, 3825–3830.

32 R. Kulmaczewski, L. J. Kershaw Cook, C. M. Pask, O. Cespedes and M. A. Halcrow, *Cryst Growth Des.*, 2022, **22**, 1960–1971.

33 Ö. Üngör, E. S. Choi and M. Shatruk, *Eur. J. Inorg. Chem.*, 2021, **2021**, 4812–4820.

34 L. J. K. Cook, R. Kulmaczewski, O. Cespedes and M. A. Halcrow, *Chem. Eur. J.*, 2016, **22**, 1789–1799.

35 R. Kulmaczewski, E. Trzop, L. J. K. Cook, E. Collet, G. Chastanet and M. A. Halcrow, *Chem. Commun.*, 2017, **53**, 13268–13271.

36 R. Kulmaczewski, E. Trzop, E. Collet, S. Vela and M. A. Halcrow, *J. Mater. Chem. C*, 2020, **8**, 8420-8429.

37 P. Chakraborty, C. Enachescu, C. Walder, R. Bronisz and A. Hauser, *Inorg. Chem.*, 2012, **51**, 9714–9722.

38 P. Chakraborty, R. Bronisz, C. Besnard, L. Guénée, P. Pattison and A. Hauser, *J. Am. Chem. Soc.*, 2012, **134**, 4049–4052.

39 C. Chong, A. Slimani, F. Varret, K. Boukheddaden, E. Collet, J.-C. Ameline, R. Bronisz and A. Hauser, *Chem. Phys. Lett.*, 2011, **504**, 29–33.

40 A. Slimani, *Phys. Rev. Lett.*, 2013, **110**, 087208.

41 P. Chakraborty, M. Sy, H. Fourati, T. Delgado, M. Dutta, C. Das, C. Besnard, A. Hauser, C. Enachescu and K. Boukheddaden, *Phys. Chem. Chem. Phys.*, 2022, **24**, 982–994.

42 F. Varret, K. Boukheddaden, C. Chong, A. Goujon, B. Gillon, J. Jeftic and A. Hauser, *Eur. Phys. Lett.*, 2007, **77**, 30007.

43 M. Chergui and E. Collet, *Chem. Rev.*, 2017, **117**, 11025–11065.

44 Y. Jiang, L. C. Liu, H. M. Müller-Werkmeister, C. Lu, D. Zhang, R. L. Field, A. Sarracini, G. Moriena, E. Collet and R. J. D. Miller, *Angew. Chem. Int. Ed.*, 2017, **56**, 7130–7134.

45 I. Krivokapic, P. Chakraborty, R. Bronisz, C. Enachescu and A. Hauser, *Angew. Chem. Int. Ed.*, 2010, **49**, 8509–8512.

46 A. Marino, P. Chakraborty, M. Servol, M. Lorenc, E. Collet and A. Hauser, *Angew. Chem. Int. Ed.*, 2014, **53**, 3863–3867.

47 R. Bertoni, M. Cammarata, M. Lorenc, S. F. Matar, J.-F. Létard, H. T. Lemke and E. Collet, *Acc. Chem. Res.*, 2015, **48**, 774–781.

48 R. Bertoni, M. Lorenc, A. Tissot, M.-L. Boillot and E. Collet, *Coord. Chem. Rev.*, 2015, **282–283**, 66–76.

49 R. Bertoni, M. Lorenc, H. Cailleau, A. Tissot, J. Laisney, M.-L. Boillot, L. Stoleriu, A. Stancu, C. Enachescu and E. Collet, *Nature Mater.*, 2016, **15**, 606–610.

50 A. Marino, M. Cammarata, S. F. Matar, J.-F. Létard, G. Chastanet, M. Chollet, J. M. Glownia, H. T. Lemke and E. Collet, *Struct. Dyn.*, 2015, **3**, 023605.

51 T. Delgado, C. Enachescu, A. Tissot, A. Hauser, L. Guenee and C. Besnard, *J. Mater. Chem. C*, 2018, **6**, 12698–12706.

52 T. Delgado, A. Tissot, C. Besnard, L. Guénée, P. Pattison and A. Hauser, *Chem. Eur. J.*, 2015, **21**, 3664–3670.

53 M. A. Halcrow, *Coord. Chem. Rev.*, 2009, **253**, 2493–2514.

54 M. A. Halcrow, *Chem. Soc. Rev.*, 2011, **40**, 4119–4142.

55 M. A. Halcrow, *Coord. Chem. Rev.*, 2005, **249**, 2880–2908.

56 L. J. Kershaw Cook, R. Mohammed, G. Sherborne, T. D. Roberts, S. Alvarez and M. A. Halcrow, *Coord. Chem. Rev.*, 2015, **289–290**, 2–12.

57 S. Brooker, *Chem. Soc. Rev.*, 2015, **44**, 2880–2892.

58 K. Ridier, G. Molnar, L. Salmon, W. Nicolazzi and A. Bousseksou, *Solid State Sciences*, 2017, **74**, A1–A22.

59 R. G. Miller, S. Narayanaswamy, J. L. Tallon and S. Brooker, *New J. Chem.*, 2014, **38**, 1932–1941.

60 K. S. Murray and C. J. Kepert, in *Spin Crossover in Transition Metal Compounds I*, eds. P. Gutlich and H. A. Goodwin, Springer, Berlin, Heidelberg, 2004, pp. 195–228.

61 H. Banerjee, M. Kumar and T. Saha-Dasgupta, *Phys. Rev. B*, 2014, **90**, 174433.

62 S. Karmakar, P. Chakraborty and T. Saha-Dasgupta, *J. Phys. Chem. C*, 2024, **128**, 16179–16188.

63 J. Kusz, R. Bronisz, M. Zubko and G. Bednarek, *Chem. Eur. J.*, 2011, **17**, 6807–6820.

64 L. J. Kershaw Cook, H. J. Shepherd, T. P. Comyn, C. Balde, O. Cespedes, G. Chastanet and M. A. Halcrow, *Chem. Eur. J.*, 2015, **21**, 4805–4816.

65 C. Enachescu, L. Stoleriu, A. Stancu and A. Hauser, *Phys. Rev. Lett.*, 2009, **102**, 257204.

66 C. Enachescu, L. Stoleriu, A. Stancu and A. Hauser, *J. Appl. Phys.*, 2011, **109**, 07B111.

67 L. Stoleriu, A. Stancu, P. Chakraborty, A. Hauser and C. Enachescu, *J. Appl. Phys.*, 2015, **117**, 17B307.

68 A.-I. Popa, L. Stoleriu and C. Enachescu, *J. Appl. Phys.*, 2021, **129**, 131101.